Journal of Experimental Botany, Vol. 70, No. 16 pp. 4305–4317, 2019
doi:10.1093/jxb/erz176 Advance Access Publication 12 April, 2019
This paper is available online free of all access charges (see https://academic.oup.com/jxb/pages/openaccess for further details)

RESEARCH PAPER

Arabidopsis glucosinolate storage cells transform into phloem fibres at late stages of development

Pascal Hunziker, Barbara Ann Halkier and Alexander Schulz*

Department of Plant and Environmental Sciences, DynaMo Center, University of Copenhagen, Thorvaldsensvej 40, 1871 Frederiksberg C, Denmark

* Correspondence: als@plen.ku.dk

Received 16 December 2018; Editorial decision 2 April 2019; Accepted 5 April 2019

Editor: Simon Turner, University of Manchester, UK

Abstract

The phloem cap of *Arabidopsis thaliana* accumulates glucosinolates that yield toxic catabolites upon damage-induced hydrolysis. These defence compounds are stored in high concentrations in millimetre long S-cells. At early stages of development, S-cells initiate a process indicative of programmed cell death. How these cells are maintained in a highly turgescent state following this process is currently unknown. Here, we show that S-cells undergo substantial morphological changes during early differentiation. Vacuolar collapse and rapid clearance of the cytoplasm did not occur until senescence. Instead, smooth endoplasmic reticulum, Golgi bodies, vacuoles, and undifferentiated plastids were observed. Lack of chloroplasts indicates that S-cells depend on metabolite supply from neighbouring cells. Interestingly, TEM revealed numerous plasmodesmata between S-cells and neighbouring cells. Photoactivation of a symplasmic tracer showed coupling with neighbouring cells that are involved in glucosinolate synthesis. Hence, symplasmic transport might contribute to glucosinolate storage in S-cells. To investigate the fate of S-cells, we traced them in flower stalks from the earliest detectable stages to senescence. At late stages, S-cells were shown to deposit thick secondary cell walls and transform into phloem fibres. Thus, phloem fibres in the herbaceous plant Arabidopsis pass a pronounced phase of chemical defence during early stages of development.

Keywords: Glucosinolates, phloem cap, phloem fibre, photoactivation, plasmodesmata, S-cell.

Introduction

Glucosinolates (GLSs) are sulfur- and nitrogen-rich compounds characteristic of the Brassicales order and required for chemical defence against a variety of attackers ranging from herbivorous insects and mammals to phytopathogenic microorganisms. Upon attack, GLSs are hydrolysed by endogenous β-glucosidases termed myrosinases, yielding toxic compounds. In *Arabidopsis thaliana* (hereafter Arabidopsis), GLSs and myrosinase accumulate in separate cells termed S-cells and myrosin idioblasts (MIs) that disrupt upon crushing, chewing, or wounding, leading to passive mixture of the two components (Kissen *et al.*, 2009; Nintemann *et al.*, 2018). Both cell types are located in the periphery of the phloem. S-cells form a cell cluster that constitutes the phloem cap between phloem and either the starch sheath of the flower stalk, pedicle, and silique replum, or the bundle sheath of petioles, mid-rib, and major veins of both rosette and cauline leaves (Koroleva *et al.*, 2000, 2010; Sarsby *et al.*, 2012). MIs are often located adjacent to S-cells at the phloem cap, but are also present in the phloem itself (Andréasson *et al.*, 2001). S-cells have been identified in roots of *Brassica napus* in a position analogous to

Abbreviations: ER, endoplasmic reticulum; FLIP, fluorescence loss in photobleaching; GLS, glucosinolate; JA, jasmonic acid; MI, myrosin idioblast; PCD, programmed cell death; PD, plasmodesma; SAM, shoot apical meristem.

Arabidopsis flower stalks and leaves (McCully *et al.*, 2008). In both Arabidopsis and *B. napus*, S-cells were identified as sulfur-rich cells by sulfur mapping using cryo-SEM/energy-dispersive X-ray analysis (Koroleva *et al.*, 2000, 2010; McCully *et al.*, 2008; Sarsby *et al.*, 2012). In Arabidopsis flower stalks, S-cells were characterized as highly elongated (>1 mm), thin-walled cells with high turgor pressure. Direct sampling of S-cell sap using a micro-capillary demonstrated that S-cells contain >100 mM GLS, accounting for 40% of the total sulfur in the stalk (Koroleva *et al.*, 2000, 2010). Sucrose levels were <10 mM, indicating that cell extracts were not contaminated by phloem sap. The high level of glucose found in the upper stem, together with a low level of GLS, could indicate that hydrolysis of GLS is triggered by the sampling process (Koroleva *et al.*, 2010). Indeed, proteomic analysis of S-cell extracts in the upper flower stalk identified the myrosinases TGG1 and TGG2 [thioglucoside glucohydrolase (TGG)] among the most abundant proteins (Koroleva and Cramer, 2011), indicating that micro-sampling disrupts not only S-cells but also MIs. Proteomic analysis of S-cell extracts further suggests that GLSs are not produced in S-cells as no GLS biosynthetic enzymes could be detected (Koroleva and Cramer, 2011). Transgenic plants stably expressing fluorophore-tagged versions of GLS biosynthetic enzymes under the control of their native promoters demonstrated that S-cells do not synthesize GLSs themselves (Li *et al.*, 2011; Nintemann *et al.*, 2018). The tagged enzymes were detected in the neighbouring starch sheath and phloem parenchyma, and also in the more distal xylem parenchyma of flower stalks. Spatial separation of GLS synthesis and accumulation indicates that GLSs are transported from sites of production to sites of storage.

The high-affinity, plasma membrane-localized GLS importers GTR1/NPF2.10, GTR2/NPF2.11, and GTR3/NPF2.9 are involved in seed loading, root exudation, intra-leaf distribution, and transport between root, shoot, and flower stalks (Nour-Eldin *et al.*, 2012; Andersen *et al.*, 2013; Andersen and Halkier, 2014; Madsen *et al.*, 2014; Jørgensen *et al.*, 2017; Xu *et al.*, 2017). Supported by the vascular localization of GTR1–GTR3, the current model suggests that GTRs mediate long-distance transport of GLSs by controlling the concentration in phloem and xylem via phloem loading and xylem retrieval (Nour-Eldin *et al.*, 2012; Madsen *et al.*, 2014, 2015). In addition to GTR-mediated transport, cell to cell transport of GLSs has been proposed to follow the symplasmic route by diffusion through plasmodesmata (PDs) (Andersen *et al.*, 2013; Madsen *et al.*, 2014; Xu *et al.*, 2017; Nintemann *et al.*, 2018). PDs are nanosized pores that connect the cytosol of adjacent cells and allow transport of photoassimilate, proteins, mRNA, ions, and signalling molecules. Small molecules and ions can freely diffuse through the cytoplasmic sleeve of PDs, while movement of proteins and mRNA is highly selective (Brunkard *et al.*, 2015). Diffusion of GLSs into S-cells via PDs would demand that S-cells and neighbouring cells are coupled by functional PDs and require a system to remove GLSs from the cytosol of S-cells to maintain a chemical gradient. Indeed, GLSs are assumed to be depleted from the cytosol and stored in vacuoles, as shown for seedlings of *Brassica juncea* (Kelly *et al.*, 1998).

S-cells have been reported to undergo programmed cell death (PCD) at early stages of development based on TUNEL (terminal deoxynucleotidyl transferase dUTP nick end labelling) of DNA double strand breaks and appearance of PCD-related features on electron micrographs (Koroleva *et al.*, 2010). At the observed stage, S-cells were still alive as they contained a turgid protoplast with intact mitochondria, plasma membrane, and vacuoles (Koroleva *et al.*, 2010). Two types of PCD can be discriminated in plants. Autolytic PCD is characterized by rapid clearance of the cytoplasm upon tonoplast rupture and corresponds to developmental PCD as observed, for example, during the differentiation of xylem vessels and fibres in Arabidopsis (van Doorn, 2011; Bollhöner *et al.*, 2012). In contrast, non-autolytic PCD is mainly found during biotic interactions as part of either the hypersensitive response or the necrotic phenomena (van Doorn, 2011). It is currently unknown which type of PCD is occurring in S-cells and for how long the protoplasts of these GLS-rich cells are maintained.

To advance our understanding of S-cells, we investigated their ultrastructure in the course of development and assessed the events of PCD using TEM. To cope with artefactual changes due to preparation for electron microscopy, we applied a recently published protocol for improved chemical fixation of fragile cells that relies on transpiration-assisted perfusion (Hunziker and Schulz, 2019). Tracing of S-cells from the earliest detectable stages of development to senescence indicates that they are maintained in an intermediary stage of differentiation serving to store GLSs prior to completion of differentiation into phloem fibres. To our knowledge, developmentally regulated transformation of one highly specialized cell such as the S-cells into another has not been described so far. We further show that S-cells are well connected to surrounding cells by PDs, and demonstrate coupling of S-cells and GLS biosynthetic cells using photoactivation and tracing of a PD-mobile dye.

Materials and methods

Plant material

Arabidopsis thaliana Col-0, the *myb28 myb29 cyp79b2 cyp79b3* mutant (Müller *et al.*, 2010), and CYP83A1-mVenus (Xu *et al.*, 2017) plants were cultivated on soil in a climate chamber under long-day conditions (16 h light, 100–140 μmol m^{-2} s^{-1}, 21 °C, 70% humidity).

Transmission electron microscopy

The adapted transpiration-assisted perfusion fixation protocol used in this study has been described in detail (Hunziker and Schulz, 2019). Briefly, inflorescence stems or rosette leaves were cut as close to the base as possible and transferred into a 1.5 ml Eppendorf tube containing freshly prepared 4% paraformaldehyde and 5% glutaraldehyde in 0.1 M sodium cacodylate buffer at pH 7.3. Stems or leaves were allowed to transpire the fixative via the xylem for 60 min at room temperature in an illuminated fume hood (Fig. 5K). The basal 3 mm end of the stems or petioles were discarded and transverse or longitudinal sections were collected in new fixative and agitated for 2 h on a rotator. Following five washing steps in 0.1 M sodium cacodylate buffer for 1 h, samples were post-fixed overnight at 4 °C in freshly prepared 0.1 M sodium cacodylate buffer at pH 7.3 containing 1% osmium tetroxide. Following five washing steps in 0.1 M sodium cacodylate buffer for

1 h, samples were dehydrated through an acetone series and infiltrated with Spurr's resin using the low viscosity kit (Electron Microscope Sciences, Hatfield, PA, USA). Samples were polymerized in a ventilated lab oven at 60±1 °C for 36 h following oriented embedding into moulds or gelatine capsules for transverse and longitudinal sectioning, respectively. Polymerized blocks were trimmed, and regions of interest were selected on crystal violet-stained semi-thin sections. Ultrathin sections were produced using a Leica EM-UC7 ultramicrotome (Leica Microsystems, Mannheim, Germany) equipped with a DiATOME diamond knife (Electron Microscope Sciences). Sections 60 nm thick were produced, flattened using chloroform, and collected onto single-slot 2 mm×1 mm nickel grids (Electron Microscope Sciences) coated with pioloform film. Sections were post-contrasted using 4% uranyl acetate in water for 3 min and Reynold's lead citrate for 5 min. Specimens were observed with a Phillips CM100 transmission electron microscope at 80 kV. Due to a slight mismatch of the offset, some images were manually corrected by applying a shading gradient over the entire image using Photoshop CC (Version 19.0, Adobe Systems Inc., San Jose, CA, USA). Images were annotated using Illustrator CC (Version 22.0.1, Adobe Systems Inc.).

Confocal microscopy

A Leica TCS SP5X confocal laser-scanning microscope (Leica Microsystems) equipped with an HCX PL APO lambda blue 20.0×0.70 IMM UV objective was used in all fluorescence microscopy experiments. Primary fluorescence of lignin was obtained by excitation using a UV laser (Coherent, Santa Clara, CA, USA) with 355 nm wavelength and a detection window for emission of fluorescence between 380 nm and 500 nm. Chlorophyll autofluorescence was recorded using the argon laser with 488 nm or 514 nm excitation and a detection window for emission of fluorescence between 650 nm and 750 nm. mVenus was excited with the 514 nm line of the argon laser set with 24% pre-set laser power and 64% AOFT gain. Emission fluorescence of mVenus was detected between 520 nm and 550 nm with 1000 mV PMT gain.

For photoactivation microscopy, flower stalks of Arabidopsis were cut at the base using a fresh razor blade and segmented in 1 cm pieces that were embedded in 6% agarose dissolved in phosphate-buffered saline (PBS) pH 7.2, and cut longitudinally into 100 µm thick sections using a Leica VT 1000 S vibratome (Leica Microsystems). The sections were immediately immersed in PBS pH 7.2 containing CMNB-caged fluorescein (Invitrogen, Carlsbad, CA, USA) at a final concentration of 20 µg ml^{-1} for 20 min in the dark (Liesche and Schulz, 2012*a*, *b*). Following five washing steps in PBS, specimens were loaded onto the microscope and the sections were screened for CYP83A1-positive cells in proximity to S-cells using the settings for imaging of mVenus. CYP83A1-mVenus-positive cells were selected as regions of interest (ROIs) for photoactivation using the built-in FRAP wizard of the Leica Application Suite software. A time series consisting of pre-photoactivation (three frames), photoactivation (60 frames), and post-photoactivation (three frames) phases was recorded at 512×512 pixels resolution using 2× zoom, a scan speed of 400 Hz, and a line average of 1. Fluorescein was imaged using the argon laser set at 488 nm with 24% pre-set laser power and 44% AOTF gain for excitation, and a detection window for emission fluorescence between 495 nm and 550 nm with 929 mV PMT gain. The UV laser was applied to ROIs in fly-mode that allows monitoring of the cell to cell movement of fluorescein simultaneously with photoactivation without a requirement to correct for background fluorescence caused by the UV laser. The UV laser used for photoactivation was set to 355 nm with 20% pre-set laser power and 100% AOTF gain. Prior to and immediately after the photoactivation sequence, high-resolution pre-photoactivation and post-photoactivation images were manually acquired at 1024×1024 pixels resolution and a line average of 16. At the end of each experiment, the entire field of view was photoactivated to ensure equal loading of the dye. For quantification of total fluorescence intensity in cells of interest over the course of photoactivation, ROIs corresponding to the CYP83A1-mVenus-positive target cell and direct neighbours were defined using Fiji (Version 2.0.0-rc-68/1.52h, www.fiji.sc).

Histochemical staining of lignin

Inflorescence stems of 8-week-old plants that were >30 cm tall and showed ripeness of the first siliques were cut at the base, segmented into 1 cm pieces, and embedded in 6% agarose in water. Sections of 100 µm thickness were prepared using a Leica VT 1000 S vibratome (Leica Microsystems) and stained with 5% phloroglucinol-HCl solution that was freshly prepared by mixing equal volumes of 10% phloroglucinol (Sigma-Aldrich Inc., St. Louis, MO, USA) in ethanol and 37% HCl. Samples were observed using a Leica DMR HC (Leica Microsystems).

Results

Ultrastructural characterization of the phloem of Arabidopsis inflorescence stems

Figure 1A shows a transverse section of a young vascular bundle. S-cells form clusters of thin-walled cells just inside the starch sheath and are easily recognized by their large width and electron-translucent cytoplasm. In contrast to the starch sheath cells, they are highly elongated (Fig. 1B). According to their position, S-cells belong to the vascular tissue and form the peripheral phloem cap. As a single layer, the starch sheath forms the boundary between vascular and ground tissue, and is clearly identified by distinctive starch-containing plastids (amyloplasts) (Fig. 1A–C, F). According to their ultrastructure, five different cell types can be distinguished within the phloem: electron-translucent sieve elements, companion cells with a dense cytoplasm, phloem parenchyma cells, MIs, and S-cells (Fig. 1A, B; Supplementary Fig. S1 at *JXB* online). The distribution of organelles along the walls of sieve elements indicates that the transpiration-assisted perfusion method was able to minimize artefacts provoked by the TEM preparation. At this distance from the shoot apical meristem (SAM; 5 mm), we have counted 5–13 S-cells, and the functional phloem consisted mostly of protophloem sieve elements (Fig. 1A).

MIs can be distinguished by the presence of large vacuoles containing an electron-dense reticular network of protein and by the high abundance of rough endoplasmic reticulum (ER) in the cytoplasm (Fig. 1A, B) (Thangstad *et al.*, 1991; Höglund *et al.*, 1992; Husebye *et al.*, 2002). As such, they are different from companion cells, which have small vacuoles and numerous free ribosomes in the cytoplasm, and from phloem parenchyma cells, which have large electron-translucent vacuoles and a less dense cytoplasm. The fact that MIs were abundant and structurally mature suggests that S-cells are functional in GLS-based defence at this stage of vascular development.

The apical ends of S-cells contain many medium-sized vacuoles and osmiophilic bodies embedded in a loose cytoplasm without obvious ribosomes (Fig. 1C). The endomembrane system consists of several Golgi bodies, enlarged smooth ER, multivesicular bodies, and vesicles. The plastids were different from both the amyloplasts of starch sheath cells and elongated chloroplasts of the phloem parenchyma, by being smaller and having only a few thylakoid membranes, but abundant plastoglobuli (Fig. 1B–D, F). The morphology of the plastids is similar to that of proplastids and plastids found in phloem parenchyma cells (Fig. 1G). However, the plastids in phloem parenchyma cells were elongated and contained more thylakoids. Examination of S-cells in sections of the basal inflorescence

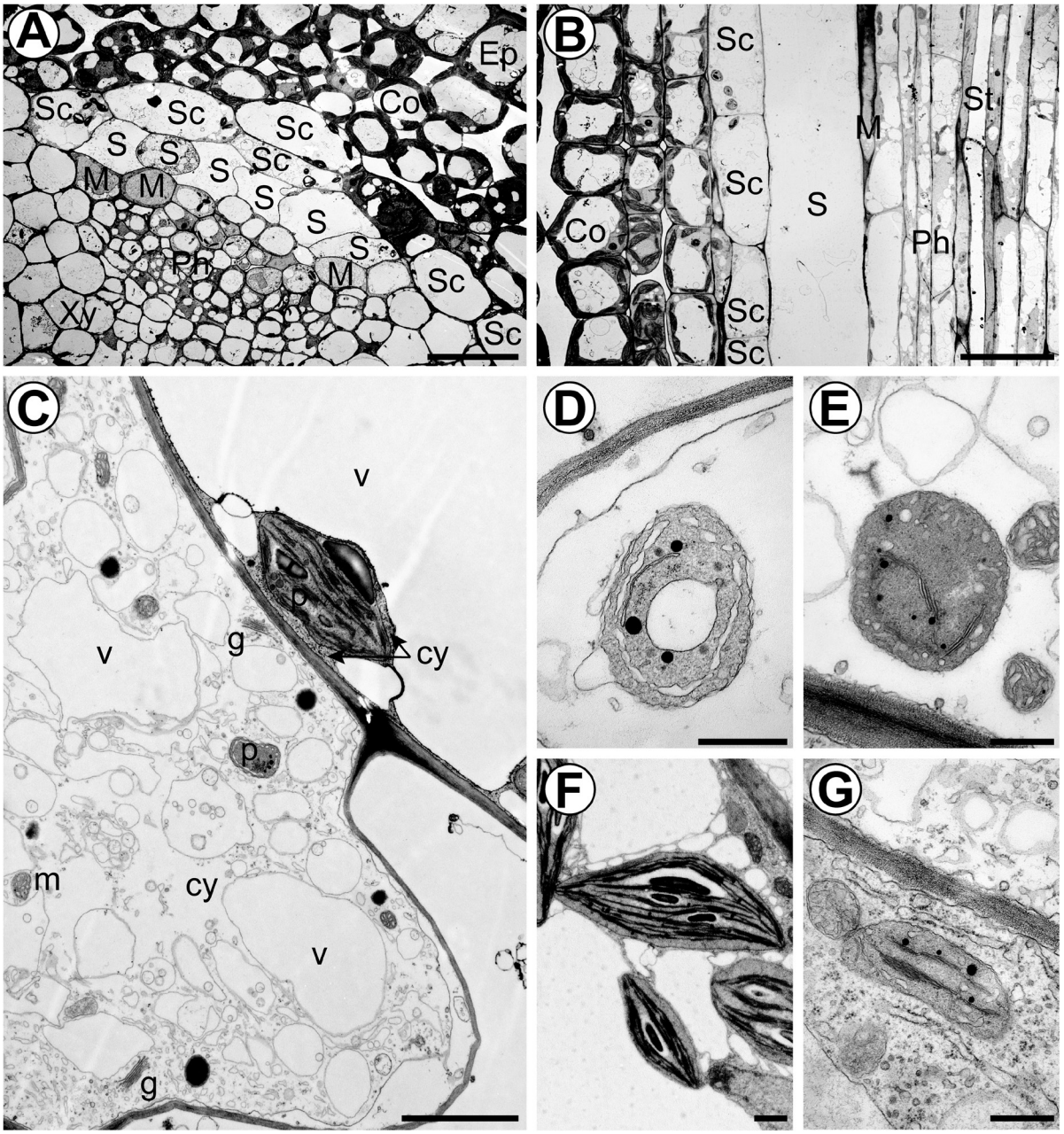

Fig. 1. Ultrastructural characteristics of S-cells in flower stalks of 6-week-old plants. (A) Overview of a vascular bundle in a transverse section 5 mm below the SAM. (B) Longitudinal section of an S-cell 5 mm below the SAM. (C) S-cell located next to a starch sheath cell with a typical amyloplast. (D) Proplastid-like structures observed in S-cell found 5 mm below the SAM. (E) Proplastid-like structures observed in S-cells found in the basal internode. (F) Amyloplasts observed in starch sheath cells. (G) Chloroplasts observed in adjacent phloem parenchyma cells. Ep, epidermis; Co, cortex; SC, starch sheath cell; S, S-cell; Ph, protophloem; Xy, protoxylem; M, myrosin idioblast; St, sieve-tube; v, vacuole; m, mitochondrion; p, plastid; g, Golgi apparatus; cy, cytosol. Scale bars (A and B) 20 μm; (C) 2 μm; (D–G) 500 nm. See also Supplementary Fig. S1 where the cell types are false colour-labelled.

stem identified similar proplastid-like structures, demonstrating that intact plastids are maintained until late stages of development (Fig. 1E). Interestingly, subcellular structures are non-uniformly distributed in the S-cell volume. On longitudinal sections, subcellular structures were more abundant at the pointed ends of the cells and discrete patches in the cell lumen that are not packed with vacuoles. As a result, abundance of subcellular structures varied between neighbouring S-cells on transverse sections (Figs 1A, 2A).

S-cells are coupled by PDs with phloem parenchyma and the starch sheath

To evaluate the symplasmic continuity between S-cells and adjacent cells, we screened common cell wall interfaces for PDs in electron micrographs of sections 5 mm from the apex. PDs were found at all interfaces except for those common with MIs (Fig. 2A; MIs not shown in this cross-section). Also, neighbouring S-cells are connected by

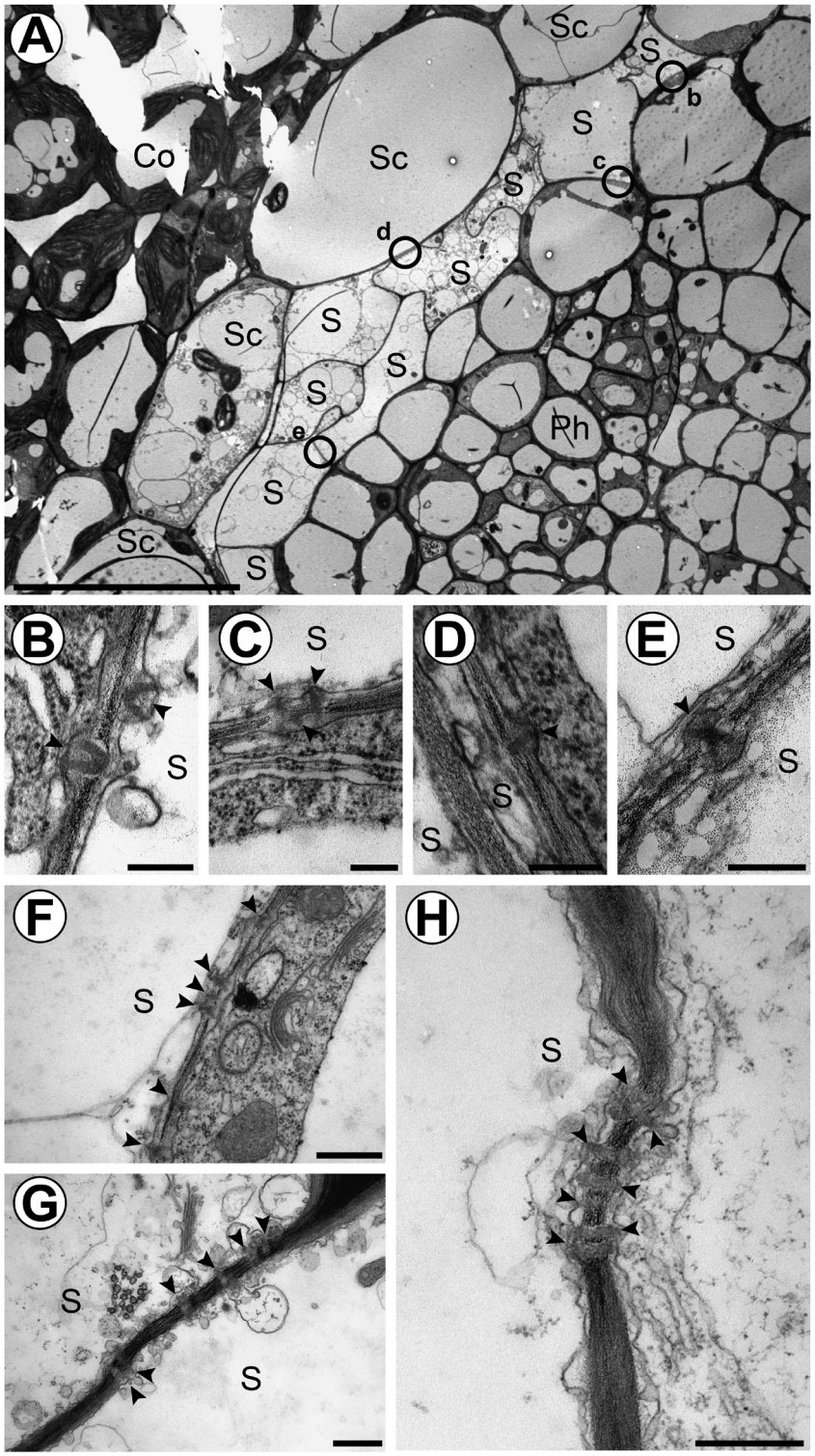

Fig. 2. TEM reveals that PDs connect S-cells to adjacent cells and organize into clusters during cell maturation. (A) Overview of a vascular bundle in a transverse section 5 mm below the SAM of flower stalks from 6-week-old plants. Circles indicate the localization of PDs shown in (B–E). (B) Cell wall interface between an S-cell and a phloem parenchyma cell. (C) Cell wall interface between an S-cell and a phloem parenchyma cell. (D) Cell wall interface between an S-cell and a starch sheath cell. (E) Cell wall interface between two adjacent S-cells. (F) Cluster of PDs found between an S-cell and a phloem parenchyma cell in a central internode. (G) Cluster of PDs found between two adjacent S-cells in the basal internode. (H) Cluster of PDs found between an S-cell and a starch sheath cell in the basal internode. Arrowheads highlight individual PDs. Ep, epidermis; Co, cortex; SC, starch sheath cell; S, S-cell; Ph, protophloem; Xy, protoxylem; Pi, pith. Scale bars (A) 20 μm; (B–E), 200 nm; (F–H) 500 nm.

PDs (Fig. 2A, E). MIs were not completely isolated, but infrequently coupled with phloem parenchyma cells. We observed both branched and unbranched PDs in the walls of S-cells (Fig. 2B, C, E, and D, H, respectively). In more basal sections, PDs could still be observed in S-cell walls, often in clusters, indicating that symplasmic continuity to

the phloem parenchyma and starch sheath is retained (Fig. 2F–H; Supplementary Fig. S3B)).

The presence of PDs in TEM micrographs is no proof of their functionality. Moreover, the size of S-cells (>1000 µm×10 µm) excludes reliable measurements of PD frequencies across the different interfaces. Furthermore, as PDs can be physiologically gated and their permeability reduced due to callose deposition and conformational changes of PD proteins, PD frequencies do not reflect the actual degree of cell coupling. Therefore, we used live cell imaging and symplasmic tracers to test functional cell coupling.

In the context of the defence function of S-cells, an important question is whether cells synthesizing GLSs are directly or indirectly linked to S-cells. Coupling can be assessed by using fluorescence redistribution after photobleaching (FRAP), fluorescence loss in photobleaching (FLIP), or photoactivation of symplasmic tracers. The first two approaches depend on a retained symplasmic pool of the pre-loaded tracer. Our first attempts using these approaches failed. It was not possible to bleach one of the huge S-cells efficiently, since the pool of fluorescein in the observed part of the target cell was immediately replenished from areas outside the field of view and neighbouring cells. Accordingly, the symplasmic pool of S-cells and neighbouring cells was virtually unlimited, indicating that all cells are well coupled.

Therefore, we chose photoactivation microscopy to test cell coupling, and monitored the intercellular flux of fluorescein upon cell-specific uncaging of CMNB-caged fluorescein (Fig. 3). To test cells that are actually involved in GLS synthesis, we utilized transgenic plants expressing *CYP83A1-mVenus* under the control of the endogenous promoter, which is a marker for biosynthesis of aliphatic GLSs (Nintemann et al., 2018)—the most prominent class of GLSs found in S-cells extracts. Consistent with previous findings, CYP83A1-mVenus localized to both starch sheath and vascular parenchyma cells, but was absent in S-cells (Fig. 3A), confirming that S-cells are unable to synthesize GLSs (Nintemann et al., 2018). Following loading of CMNB-caged fluorescein onto longitudinal sections in radial orientation, individual CYP83A1-positive cells were selected as targets for photoactivation with a UV-laser (Fig. 3B, white outlines). Right from the start of photoactivation, fluorescein appeared in S-cells and non-photoactivated cells of the starch sheath and phloem (Fig. 3C, D; Supplementary Video S1). There was no obvious spread of the tracer from the starch sheath cells to the immediate neighbouring cortex cells, indicating that symplasmic coupling between starch sheath and cortex is more restricted. Quantification of fluorescence intensity revealed that S-cells accumulate fluorescein with dynamics fitting the logistic function (Fig. 3E). Fluorescein accumulation in photoactivated cells was saturated at 39 s with a half-time of accumulation at ~9±1 s, in contrast to twice that value in S-cells. As a control, the mounting medium did not show a significant increase in fluorescence. In conclusion, PDs interconnecting S-cells and GLS-producing starch sheath and phloem parenchyma cells appear highly functional.

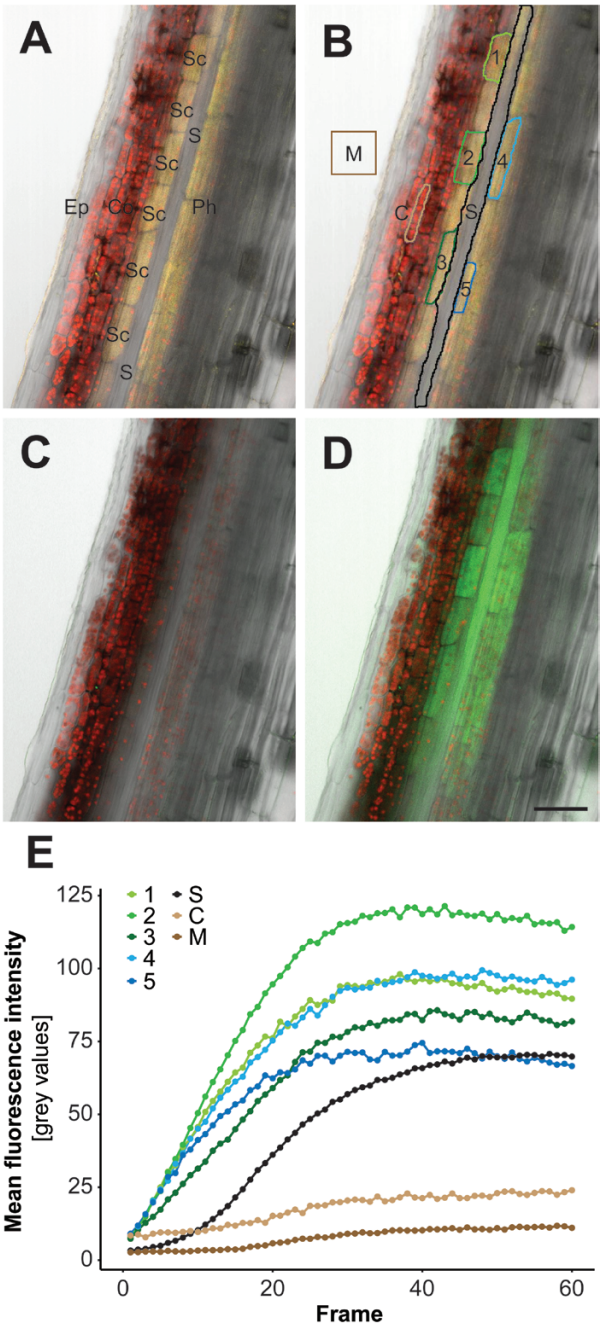

Fig. 3. Cell coupling between CYP83A1-positive cells and S-cells revealed by photoactivation and tracing of CMNB-caged fluorescein. (A) Overlay of chlorophyll autofluorescence (red), transmission light (grey), and mVenus (yellow) channels of a longitudinal section through an apical inflorescence stem expressing *pCYP83A1:CYP83A1-mVenus*. CYP83A1-mVenus is localized to starch sheath and phloem parenchyma cells, but not to adjacent S-cells. (B) ROIs selected for photoactivation of CMNB-caged fluorescein in CYP83A1-positive cells (cells numbered 1–5) and quantification of cell coupling (M, C, and S). (C) Overlay of high-resolution pre-photoactivation images of chlorophyll autofluorescence (red), transmission light (grey), and fluorescein (green) channels. (D) Overlay of high-resolution post-photoactivation images of chlorophyll autofluorescence (red), transmission light (grey), and fluorescein (green) channels. (E) Quantification of mean fluorescence intensity of photoactivated target cells 1–5 and non-photoactivated cells of interest including S-cells (S), imaging medium (M), and a cortical cell (C) over the course of photoactivation as shown in Supplementary Video S1. Colours match the ROIs outlined in (B). Ep, epidermis; Co, cortex; SC, starch sheath; S, S-cell; phloem. Scale bar=50 µm.

Differentiation and cell fate of S-cells

Considering that S-cells were reported to undergo PCD, we sought to follow the development of S-cells from their first identification below the SAM to senescence in order to resolve their cell fate. Figure 4 depicts a longitudinal section through the apical 550 μm of a 6-week-old inflorescence stem. In this region, the morphology and ultrastructure of S-cells were investigated by TEM. S-cells were identified according to their characteristic localization between the starch sheath and the vascular procambium. Already at 200 μm distance from the SAM (third internode), S-cells were spindle-like cells overlapping each other at their pointed ends (Fig. 4B). S-cells contained a prominent nucleus and a large central vacuole surrounded by a dense cytoplasm at the cell periphery and tips (Fig. 4C–E). Nuclei were larger than those in neighbouring cells and contained high amounts of euchromatin, indicating high transcriptional activity

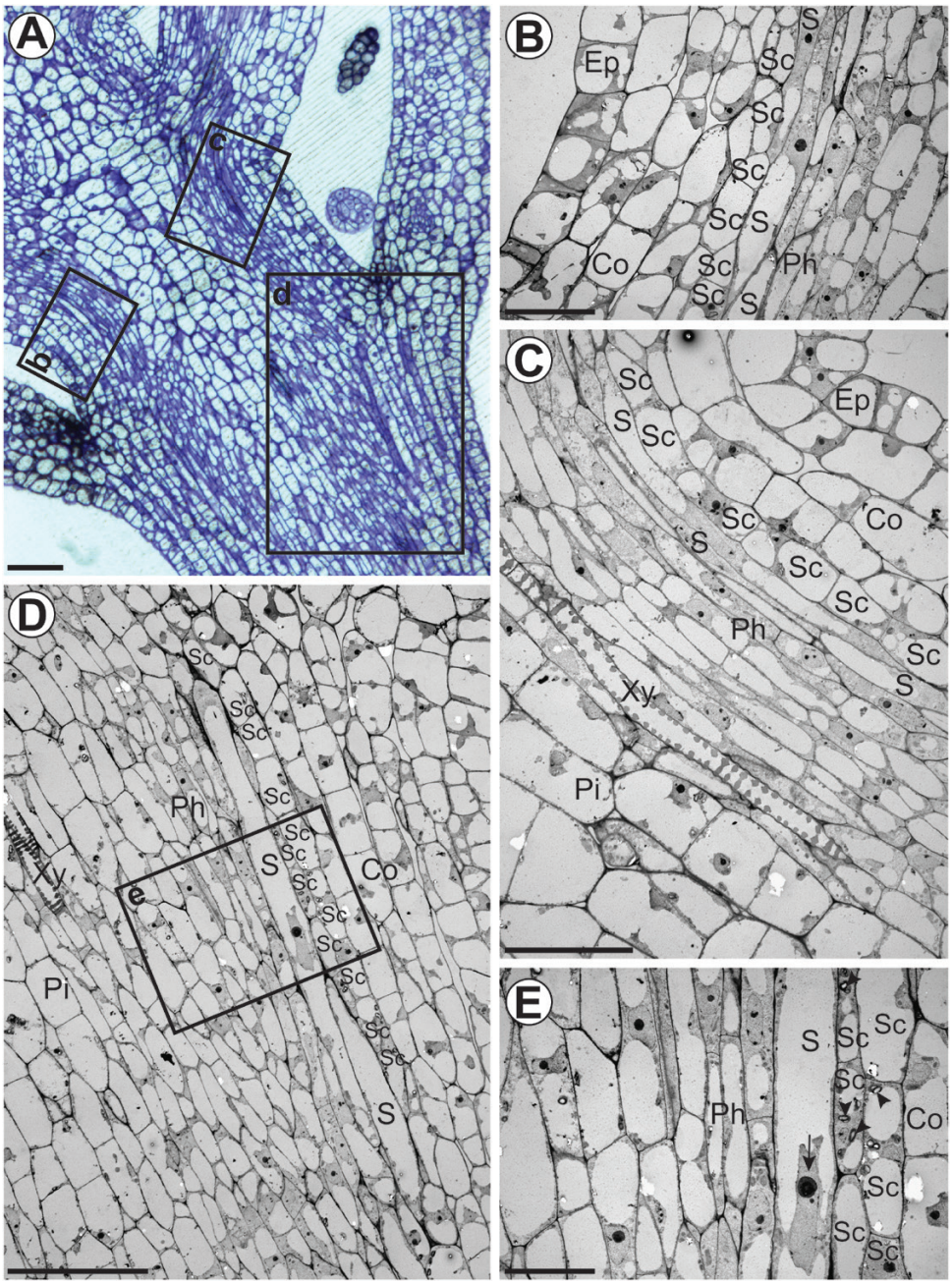

Fig. 4. Early developmental stages of S-cells in Arabidopsis inflorescence stems. (A) Light microscopic image of a crystal violet-stained longitudinal semi-thin section through the generative SAM displaying the third to fifth internode. Rectangles represent ROIs shown in (B–D). (B–D) Electron micrographs of S-cell precursors in the third, fourth, and fifth internode, respectively (200, 350, and 500 μm from the SAM). Extensively elongated precursor cells are consistently located between the starch sheath and protophloem. Precursor S-cells are equipped with a full set of organelles including a single, centrally arranged nucleus, large vacuoles, and electron-dense cytoplasm. The specimen shown in (D) has been sectioned slightly oblique. (E) Higher magnification of the region outlined in (D). The starch sheath is characterized by the presence of amyloplasts (arrowheads). Note the high amount of euchromatin in the large nucleus of the S-cell (arrow). Ep, epidermis; Co, cortex; SC, starch sheath cell; S, S-cell; Ph, protophloem; Xy, protoxylem; Pi, pith. Scale bars (A), (C), (D), 40 μm; (B), (E) 20 μm. (This figure is available in colour at *JXB* online.)

(Fig. 4E). At early stages, S-cells contained the regular complement of organelles including chloroplasts. Smaller sized plastids similar to those found at 5 mm distance from the SAM were also observed. No osmiophilic bodies, multivesicular bodies, or vesicles were observed, indicating that these structures emerge at later stages of differentiation. As S-cells mature, the cytoplasm becomes looser and the central vacuole seems to be replaced by many medium sized vacuoles (compare Fig. 1A, B). Even in fully differentiated S-cells at the stem base, a nucleus could be detected (Supplementary Fig. S3A, B). To sum up, S-cells form chains of elongated and long tapering cells that differentiate and specialize within the first 5 mm from the shoot apex. Differentiation includes the remodelling of plastids, disappearance of free and ER-bound ribosomes, as well as the formation of osmiophilic bodies, multivesicular bodies, vesicles, and branched PDs.

Transverse sections at different heights of the flower stalk reveal that the location and number of S-cells do not change throughout the stalk, as long as the siliques are immature (Fig. 5). Lignin autofluorescence at 365 nm excitation identifies the lignification process in the xylem and the development of interfascicular fibres already at 5 mm and 5 cm from the apex, respectively (Fig. 5A–D). However, starting with the opening of the oldest siliques, the walls of phloem cap cells, just inside the starch sheath, start to lignify as well (Fig. 5I, J, N–P). This location coincides with the location of the S-cells throughout the flower stalk. The presence of lignin in autofluorescent cell walls was confirmed by histochemical staining with phloroglucinol-HCl (Fig. 5L–P). The ultrastructure of S-cells that start to form secondary cell walls is similar to that of neighbouring S-cells and includes mitochondria, plastids, and vacuoles (Supplementary Fig. S3A). The start of lignification does not seem to be synchronized across the stem but, eventually, all S-cells have lignified cell walls (Fig. 5I).

As isothiocyanates, which are products of GLS hydrolysis, have been shown to induce transcriptional reprogramming including cell death responses (Kissen *et al.*, 2016), the question arises of whether the high cellular level of GLSs triggers the PCD-related morphological changes of S-cells. Therefore, we compared flower stalks of the wild type and GLS-deficient *myb28 myb29 cyp79b2 cyp79b3* mutants (Fig. 6). No differences were observed in the ultrastructure or number of S-cells in the GLS-deficient mutants, excluding a causal role for GLSs in the differentiation process of this cell type.

To study the distribution of S-cells in other organs, we investigated their ultrastructure in rosette leaves. Sections of the petiole and the midrib showed phloem caps that contained both fibre cells and S-cells in the phloem cap. No S-cells or fibres were detected in minor veins (Supplementary Fig. S2).

Discussion

GLSs might diffuse into S-cells through PDs

Our results unambiguously show the presence of PDs in all cell wall interfaces of S-cells except for those shared with MIs (Fig. 2). Detection of PDs in basal regions of the flower stalk indicates that PDs are maintained until stem senescence (Fig. 2F–H). Hence, S-cells are not completely isolated like guard cells that lack PDs at mature stages (Wille and Lucas, 1984). The observation of branched PDs implies that S-cells generate new PDs in the course of development because, in contrast to unbranched PDs which are produced during cell division, branched PDs are formed thereafter and hence are referred to as secondary PDs (Burch-Smith *et al.*, 2011). Our initial FLIP experiments to test PD functionality failed due to a virtually unlimited tracer pool. This is explained by the enormous size of S-cells and the fact that for microscopy of 3D tissue it was necessary to work with longitudinal sections, allowing for unintended tracer exchange between mounting medium and cells damaged by preparation. In contrast to FRAP or FLIP, photoactivation of pre-loaded tracer is direct evidence for intercellular tracer movement (Liesche and Schulz, 2012*a*). Coupling of S-cells and GLS biosynthetic cells was specifically shown by tracing the movement of fluorescein that has been photoactivated in CYP83A1-positive cells into S-cells (Fig. 3). Imaging required photoactivation in more than one biosynthetic cell to achieve adequate signal in S-cells. The fact that PD allowed dye diffusion indicates that PDs are not occluded by wound callose due to tissue preparation. High coupling of GLS biosynthetic cells and S-cells suggests that GLSs may be transported to S-cells via the symplasm. This finding is supported by the fact that the profile of GLSs of the S-cell content matches the GLS composition of the entire stem tissue (Koroleva *et al.*, 2010), indicating non-selective transport of GLSs. Absence of GTR1–GTR3 in S-cells would indirectly support the symplasmic transport model and will be explored in future experiments by detailed analysis of GTR1–GTR3 localization. The cellular localization within the vascular tissue has so far only been shown for GTR3 that localizes to companion cells of the root (Wang and Tsay, 2011). One benefit of symplasmic GLS transport is that it would be regulated by the strength of the respective GLS sinks. However, movement of fluorescein only proves that photoassimilates such as sucrose—known to be translocated via the symplasm—are able to be transported (Liesche and Schulz, 2012*a*). Direct proof for movement of GLSs through PDs remains to be demonstrated in future experiments using fluorescent GLSs.

S-cells are similar to phloem fibre initials

S-cells have previously been proposed to be structurally and functionally related to unbranched non-articulated laticifer cells (Koroleva *et al.*, 2010). Laticifers are long thin-walled cells that form tube systems and store an emulsion termed latex that contains active defence compounds (e.g. alkaloids and terpenes), which are released upon wounding or injury by herbivores (Pickard, 2008). Similar to S-cells in Arabidopsis, laticifers are associated with the vasculature (Koroleva *et al.*, 2010). However, laticifers have so far not been reported in the entire order of the Capparales (Hagel *et al.*, 2008). Moreover, S-cells are able to deposit thick secondary cell walls that contain significant amounts of lignin (Fig. 5). This feature is rather characteristic for sclerenchyma (e.g. fibres, which are

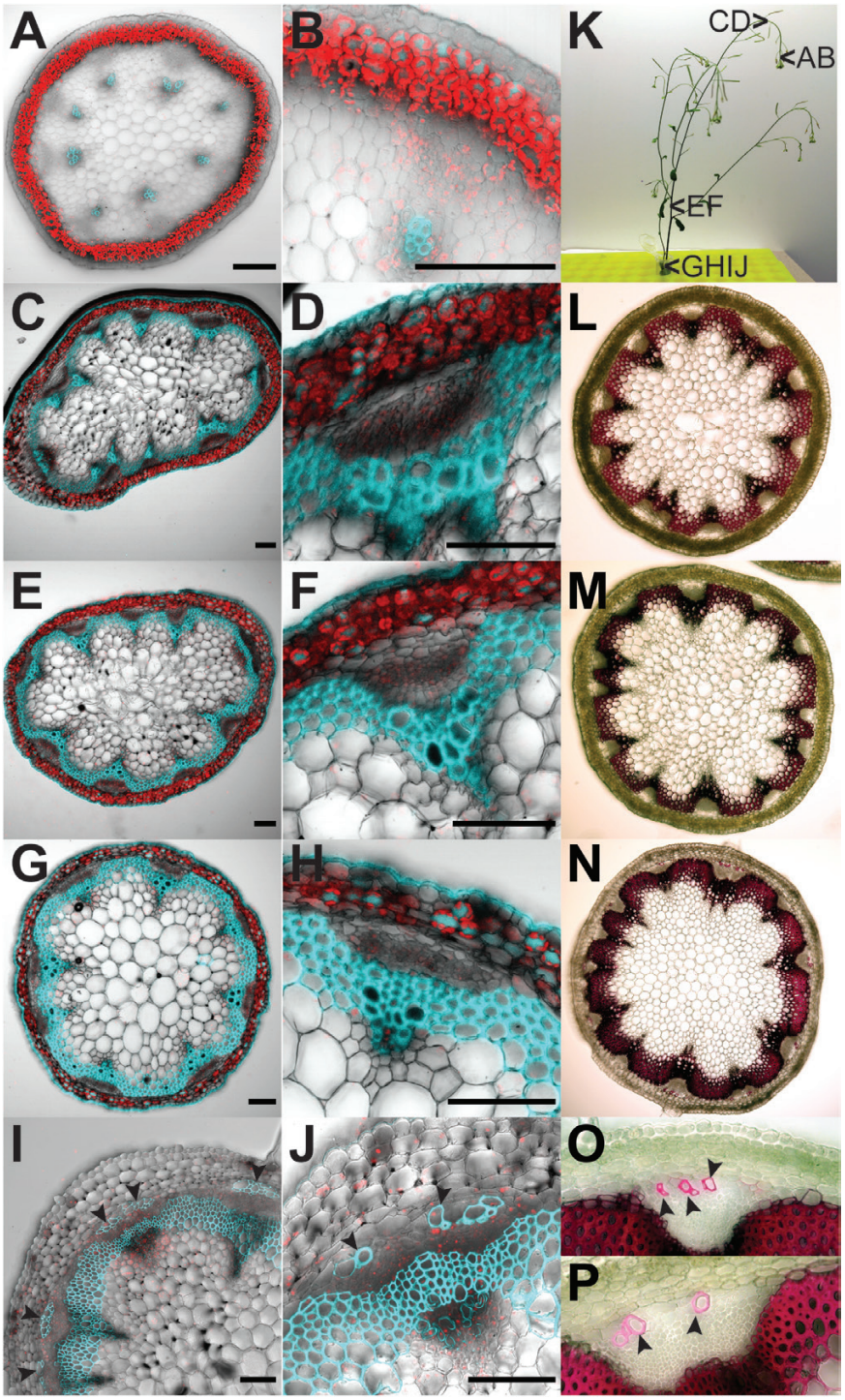

Fig. 5. Lignification of S-cells. (A–J) Overlays of confocal images depicting chlorophyll in red and lignin in cyan in transverse sections of flower stalks from 6-week-old (A–H) and 8-week-old (I and J) wild-type plants of ~10 cm and 30 cm height, respectively. Sections were taken at 5 mm distance from the SAM (A, B), at 5 cm distance from the SAM (C, D), the second internode (E, F), and the third internode at the very base of the flower stalk (G, H) as depicted in (K). (A) Lignin is found exclusively in the xylem. (B) Zoom-in on a single vascular bundle from (A). (C) Lignification of interfascicular fibres is initiated at ~5 cm from the SAM. (D) Zoom-in on a single vascular bundle from (C). (E) Lignification of interfascicular bundles is intensified in the second internode. (F) Zoom-in on a single vascular bundle from (E). (G) Lignification in the basal internode. (H) Zoom-in on a single vascular bundle from (G). Note that S-cells are not lignified at that stage. (I) Lignification of S-cells at the phloem cap is initiated at the very base of flower stalks from 8-week-old plants showing ripeness of the first siliques. (J) Zoom-in of a single vascular bundle from (I). Note that not all S-cells started to lignify at this stage. (K) Photograph of a 6-week-old (left) and an 8-week-old (right) plant. Arrowheads depict the position of sections shown in this figure. (L–P) Phloroglucinol-HCl staining of transverse sections from flower stalks of 8-week-old wild-type plants confirms the deposition of lignin in S-cells. Sections were taken at 5 cm distance from the SAM (L) and at the top (M) and bottom (N–P) of the basal internode as depicted in (K). Lignin is depicted in red. (L) Lignification of interfascicular fibres is consistent with the pattern of lignin autofluorescence observed in (C) and (D). (M) No S-cells were lignified in the top part of the basal internode. (N) Lignin is found in S-cells at the phloem cap, confirming that the autofluorescence observed in (I) and (J) is not due to other compounds. (O and P) Zoom-in on single vascular bundles from (N) Note that the pattern of lignification at the phloem cap is comparable with that of (I) and (J). Lignified S-cells are marked by arrowheads. Scale bars=250 μm.

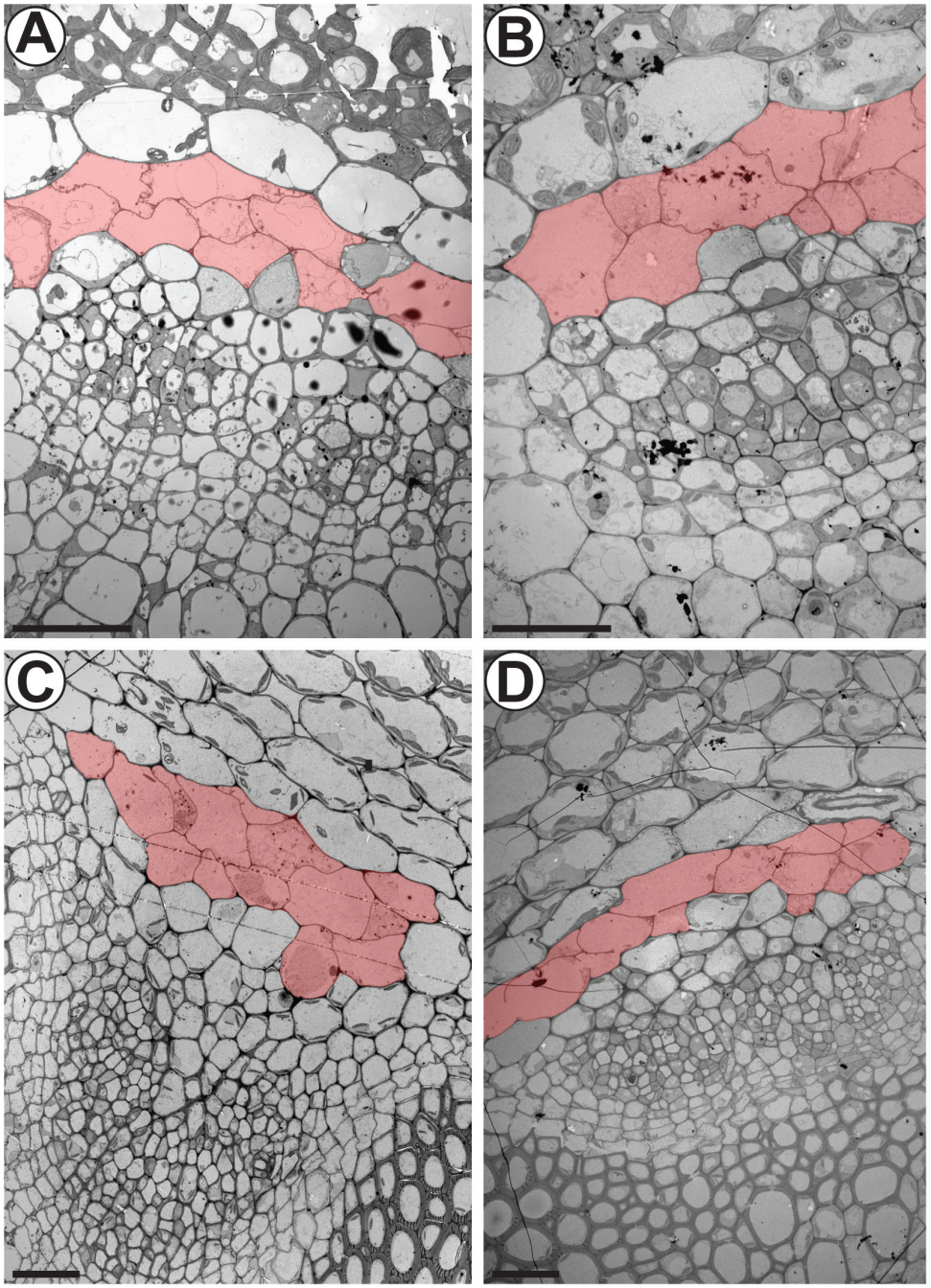

Fig. 6. The ultrastructure of S-cells is not affected in GLS-deficient *myb28 myb29 cyp79b2 cyp79b3* mutant plants. (A and B) Electron micrographs showing the phloem cap of vascular bundles in the top 5 mm of inflorescence stems from 6-week-old (A) wild-type and (B) mutant plants. (C and D) Electron micrographs showing the phloem cap of vascular bundles in the basal 5 mm of inflorescence stems from 6-week-old (C) wild-type and (D) mutant plants. S-cells are false-coloured in red according to their characteristic ultrastructure and size. Scale bars=20 μm.

supporting elements in those parts of a plant that are no longer elongating) (Evert, 2006). In many dicotyledons, the phloem cap is characterized by primary phloem fibres (Esau, 1969). Tracing the lignification process in transverse sections along the Arabidopsis flower stalk revealed that S-cells only deposit lignin in the bottom 5 mm of flower stalks that were taller than 30 cm, coinciding with silique senescence (Fig. 5L–P). Lignification of xylem vessels precedes lignification of interfascicular fibres and S-cells (Fig. 5A, B). Further down the stalk, lignification of interfascicular fibres is initiated and intensifies towards the stem base (Fig. 5C–J). Previous studies on interfascicular fibre differentiation identified the homeodomain-leucine zipper protein *IFL1* as a transcription factor gene that specifically impedes their lignification, leading to inflorescence stems that could no longer stand erect (Zhong *et al.*, 1997; Zhong and Ye, 1999). Interestingly, the authors reported that the phloem cap was lignified at the base of the flower stalk independently of *IFL1* and referred to these cells as phloem fibres (Zhong *et al.*, 1997). The phloem fibres exactly match the location of S-cells, namely between the starch sheath and phloem of each vascular bundle (Zhong *et al.*, 1997; Koroleva *et al.*, 2010). Phloem fibres corresponding

to the location of S-cells have also been described by other research groups (Altamura *et al.*, 2001; Sehr *et al.*, 2010). Consistent with our findings, the phloem cap was found to be lignified at sites of secondary growth, namely the basal part and nodes of the flower stalk (Sehr *et al.*, 2010).

Phloem fibres in economically important fibre crops such as hemp and flax are often only recognized when they possess a thickened secondary cell wall, while the thin-walled fibre initials escape detection (Evert, 2006; Chernova and Gorshkova, 2007). The morphology of S-cells (Figs 1, 2A) is reminiscent of fibre initials in flax (Ageeva *et al.*, 2005). Phloem fibres such as those found in flax and hemp are of procambial origin (Chernova and Gorshkova, 2007). Our results suggest that S-cells are derived from the procambium as they are located just inside the starch sheath, which is forming the border between cells of vascular and ground tissue origin (Fig. 4). Interestingly, we found MIs at the phloem cap and within the phloem (Figs 1A, 2A), indicating that MIs are also of procambial origin in the flower stalk in contrast to their origin from ground meristem cells in leaves (Li and Sack, 2014; Shirakawa *et al.*, 2016).

Following the coordinated growth phase of fibre initials in flax and hemp, the cells further elongate intrusively by tip or intercalary growth (Ageeva *et al.*, 2005; Evert, 2006; Snegireva *et al.*, 2015). Tip growth is characterized by the appearance of small cells, which represent transections of the intrusively growing tips, among the wider, not elongating parts of fibre initials (Evert, 2006). We observed a similar pattern in transverse sections of S-cells, indicating intrusive tip growth (Figs 1A, 2A). Fibre initials in flax and hemp become multinucleate during intrusive growth (Evert, 2006), which was not observed for S-cells. The clustered appearance of PDs in S-cells of the basal flower stalk might indicate that these structures become pit fields upon lignification as reported for phloem fibres in other species (Fig. 2F–H; Supplementary Fig. S3).

Assessment of PCD events during S-cell differentiation

S-cells have been suggested to undergo PCD during early stages of development, observed as condensation of chromatin in nuclei and swelling of chloroplasts (Koroleva *et al.*, 2010). Using an improved fixation protocol for TEM, we found that S-cells contained intact plastids and mitochondria with normal appearance at all stages of development (Fig. 1), indicating that some of the previously reported PCD-related features of S-cells may have originated from insufficient fixation. The plastids contained only a few thylakoids but abundant plastoglobuli, indicating involvement in lipid metabolism and storage (Schulz *et al.*, 1998). Furthermore, we detected numerous Golgi bodies that may serve to maintain the plasma membrane and vacuoles. Despite significant structural changes of the vacuole at early stages of differentiation, the tonoplast of S-cells is not ruptured at least until the initiation of lignification at very late stages (Figs 1, 2; Supplementary Fig. S3). Both absence of tonoplast rupture and rapid clearance of the cytoplasm indicate that S-cells are arrested at an early stage of PCD where the tonoplast is extremely turgid but not yet allowed to collapse. The developmental events in S-cells support an autolytic process similar to PCD of xylem fibres (van Doorn, 2011; Bollhöner *et al.*, 2012). This classification is supported by the high vacuole to cytoplasm ratio in S-cells (Koroleva *et al.*, 2010). Because of the large size of S-cells, nuclei were difficult to find in TEM micrographs. In contrast to the previously observed chromatin condensation in S-cells (Koroleva *et al.*, 2010), that detected in our study did not show any indication of PCD at the observed stage of development (Supplementary Fig. S3). Autolytic PCD starts with the appearance of small vacuoles that merge and thereby replace the cytoplasm gradually, leading to disappearance of considerable amounts of organelles (van Doorn, 2011). Hence, S-cells might initiate autolytic PCD early in development but maintain their protoplast and a nucleus at least until the stage of lignification (Supplementary Fig. S3A, B). This finding is consistent with xylem vessel and xylem fibre differentiation where the secondary cell wall is formed prior to vacuolar collapse (Bollhöner *et al.*, 2012). The presence of functional plasmodesmata together with the massive transcriptional reprogramming necessary for cell wall deposition are not compatible with the view that S-cells complete PCD before finalization of fibre transformation.

Which factors confer the initial commitment of S-cells to store GLSs?

Accumulation of GLSs in S-cells coincides with the initiation of PCD occurring in the top 5 mm of the flower stalk and is characterized by loosening of the cytoplasm and vacuolar structures (Figs 1, 4). The observed lightening of the cytoplasm is accompanied by the appearance of distinctive plastids and osmiophilic bodies (Fig. 1). Similar features have been described for fibre initials of flax prior to synthesis of the secondary cell wall (Chernova and Gorshkova, 2007), indicating that S-cells reflect an intermediary stage of normal phloem fibre differentiation that is suitable for high accumulation of GLSs. In contrast, it has been proposed that the high accumulation of GLSs in S-cells might induce PCD (Koroleva *et al.*, 2010). It is known that some GLS hydrolysis products trigger transcriptional reprogramming including cell death responses (Kissen *et al.*, 2016). As the ultrastructure of S-cells in GLS-deficient *myb28 myb29 cyp79b2 cyp79b3* mutants is identical to that of the wild type, S-cells obviously differentiate independently of the presence of GLSs and hydrolysis products (Fig. 6). Moreover, our data show that GLSs, which are negatively charged molecules, are not required as a driving force of the massive elongation of S-cells as the length of S-cells is also unaffected in GLS-deficient mutants (data not shown). Hence, high accumulation of GLSs neither induces the observed PCD-related structural changes of S-cells nor is required for extensive cell elongation, indicating that other factors determine the differentiation of S-cells. Future experiments will be required to identify the transcription factors involved in the differentiation of S-cells from procambial initials.

Transformation of S-cells into phloem fibres

The transformation of S-cells into phloem fibres indicates that S-cells can switch from GLS-based chemical to lignin-based

mechanical defence as lignification of cell walls contributes to plant defence (Rogers and Campbell, 2004). GLS-based chemical defence is most active in the top 5 mm of the flower stalk (Koroleva *et al*., 2010), which is the softest part of the stem and most vulnerable to attacks as only little lignin is present (Fig. 5A, B). Lignin-based mechanical defence is only realized in the bottom 5 mm of the flower stalk, which is subjected to high tension forces, indicating a role in load bearing (Fig. 5I–P). In addition to their support function, the phloem fibres might play a role in defence against herbivores that snap off entire flower stalks while feeding and form a mechanical defence barrier, for instance against phloem-feeding insects.

The transformation of S-cells into phloem fibres appears to underlie developmental regulation linked to age-related senescence. Age-related senescence is known to be promoted by endogenous oxylipids including the hormone jasmonic acid (JA), which is also involved in wound signalling and resistance to some pests (Hu *et al*., 2017). Mutants with high constitutive levels of JA display lignification of S-cells at stages of development where no lignification was observed in the wild type (Matschi *et al*., 2015; Lin *et al*., 2016). The lignification phenotype is rescued by abolishment of JA synthesis or signalling via mutation of *AOS* and *COI1*, respectively, indicating that phloem fibre lignification is initiated by JA. Interestingly, precocious lignification of S-cells is accompanied by a severe reduction of plant height that is also rescued in the *aos* and *coi1* genetic backgrounds (Sehr *et al*., 2010; Matschi *et al*., 2015; Lin *et al*., 2016). The reduction in plant height could result from the mechanical restriction of cell elongation due to precocious lignification of fibres. Alternatively, reduced stem elongation could simply result from the JA-dependent deregulation of cambium initiation and activity (Sehr *et al*., 2010). Future studies will be directed towards the identification of molecular mechanisms underlying the JA-dependent transformation of S-cells.

In conclusion, the study provides a detailed characterization of the giant, GLS-containing S-cells that execute a protective role in the phloem cap. It can be speculated that the functionality of plasmodesmata, as shown here, is a prerequisite for the transformation of this particular cell type into fibre cells by supplying metabolites for cell wall deposition.

Supplementary data

Supplementary data are available at *JXB* online.

Fig. S1. False colour-labelled copies of Fig. 1A and B.

Fig. S2. Ultrastructural characterization of S-cells in rosette leaves.

Fig. S3. The protoplast of S-cells is preserved until the formation of secondary cell walls.

Video S1. Cell coupling between CYP83A1-positive cells and S-cells revealed by photoactivation and tracing of CMNB-caged fluorescein.

Acknowledgements

This work was funded by the Danish National Research Foundation (DNRF grant 99). All images were acquired at the Center for Advanced Bioimaging Denmark (CAB). We are grateful to Catherine Anne Skrzynski Nielsen, Michael Hansen, and Helle Juel Martens for technical assistance and expertise. Meng Li is thanked for discussions regarding myrosin idioblasts. No competing interests to declare.

Author contributions

AS, BAH, and PH designed the experiments. AS and PH acquired and analysed the data. AS, BAH, and PH wrote the manuscript.

References

Ageeva MV, Petrovská B, Kieft H, Sal'nikov VV, Snegireva AV, van Dam JE, van Veenendaal WL, Emons AM, Gorshkova TA, van Lammeren AA. 2005. Intrusive growth of flax phloem fibers is of intercalary type. Planta **222**, 565–574.

Altamura MM, Possenti M, Matteucci A, Baima S, Ruberti I, Morelli G. 2001. Development of the vascular system in the inflorescence stem of Arabidopsis. New Phytologist **151**, 381–389.

Andersen TG, Halkier BA. 2014. Upon bolting the GTR1 and GTR2 transporters mediate transport of glucosinolates to the inflorescence rather than roots. Plant Signaling & Behavior **9**, e27740.

Andersen TG, Nour-Eldin HH, Fuller VL, Olsen CE, Burow M, Halkier BA. 2013. Integration of biosynthesis and long-distance transport establish organ-specific glucosinolate profiles in vegetative Arabidopsis. The Plant Cell **25**, 3133–3145.

Andréasson E, Bolt Jørgensen L, Höglund AS, Rask L, Meijer J. 2001. Different myrosinase and idioblast distribution in Arabidopsis and *Brassica napus*. Plant Physiology **127**, 1750–1763.

Bollhöner B, Prestele J, Tuominen H. 2012. Xylem cell death: emerging understanding of regulation and function. Journal of Experimental Botany **63**, 1081–1094.

Brunkard JO, Runkel AM, Zambryski PC. 2015. The cytosol must flow: intercellular transport through plasmodesmata. Current Opinion in Cell Biology **35**, 13–20.

Burch-Smith TM, Stonebloom S, Xu M, Zambryski PC. 2011. Plasmodesmata during development: re-examination of the importance of primary, secondary, and branched plasmodesmata structure versus function. Protoplasma **248**, 61–74.

Chernova TE, Gorshkova TA. 2007. Biogenesis of plant fibers. Russian Journal of Developmental Biology **38**, 221–232.

Esau K. 1969. The phloem. Berlin, Stuttgart: Gebr. Borntraeger.

Evert RF. 2006. Esau's plant anatomy: meristems, cells, and tissues of the plant body: their structure, function, and development. Hoboken, NJ: John Wiley & Sons, Inc.

Hagel JM, Yeung EC, Facchini PJ. 2008. Got milk? The secret life of laticifers. Trends in Plant Science **13**, 631–639.

Höglund A-S, Lenman M, Rask L. 1992. Myrosinase is localized to the interior of myrosin grains and is not associated to the surrounding tonoplast membrane. Plant Science **85**, 165–170.

Hu Y, Jiang Y, Han X, Wang H, Pan J, Yu D. 2017. Jasmonate regulates leaf senescence and tolerance to cold stress: crosstalk with other phytohormones. Journal of Experimental Botany **68**, 1361–1369.

Hunziker P, Schulz A. 2019. Transmission electron microscopy of the phloem with minimal artefacts. Methods in Molecular Biology (in press).

Husebye H, Chadchawan S, Winge P, Thangstad OP, Bones AM. 2002. Guard cell- and phloem idioblast-specific expression of thioglucoside glucohydrolase 1 (myrosinase) in Arabidopsis. Plant Physiology **128**, 1180–1188.

Jørgensen ME, Xu D, Crocoll C, Ramírez D, Motawia MS, Olsen CE, Nour-Eldin HH, Halkier BA. 2017. Origin and evolution of transporter substrate specificity within the NPF family. eLife **6**, e19466.

Kelly PJ, Bones A, Rossiter JT. 1998. Sub-cellular immunolocalization of the glucosinolate sinigrin in seedlings of *Brassica juncea*. Planta **206**, 370–377.

Kissen R, Øverby A, Winge P, Bones AM. 2016. Allyl-isothiocyanate treatment induces a complex transcriptional reprogramming including

heat stress, oxidative stress and plant defence responses in *Arabidopsis thaliana*. BMC Genomics **17**, 740.

Kissen R, Rossiter JT, Bones AM. 2009. The 'mustard oil bomb': not so easy to assemble?! Localization, expression and distribution of the components of the myrosinase enzyme system. Phytochemistry Reviews **8**, 69–86.

Koroleva OA, Cramer R. 2011. Single-cell proteomic analysis of glucosinolate-rich S-cells in *Arabidopsis thaliana*. Methods **54**, 413–423.

Koroleva OA, Davies A, Deeken R, Thorpe MR, Tomos AD, Hedrich R. 2000. Identification of a new glucosinolate-rich cell type in Arabidopsis flower stalk. Plant Physiology **124**, 599–608.

Koroleva OA, Gibson TM, Cramer R, Stain C. 2010. Glucosinolate-accumulating S-cells in Arabidopsis leaves and flower stalks undergo programmed cell death at early stages of differentiation. The Plant Journal **64**, 456–469.

Li J, Kristiansen KA, Hansen BG, Halkier BA. 2011. Cellular and subcellular localization of flavin-monooxygenases involved in glucosinolate biosynthesis. Journal of Experimental Botany **62**, 1337–1346.

Li M, Sack FD. 2014. Myrosin idioblast cell fate and development are regulated by the Arabidopsis transcription factor FAMA, the auxin pathway, and vesicular trafficking. The Plant Cell **26**, 4053–4066.

Liesche J, Schulz A. 2012*a*. In vivo quantification of cell coupling in plants with different phloem-loading strategies. Plant Physiology **159**, 355–365.

Liesche J, Schulz A. 2012*b*. Quantification of plant cell coupling with three-dimensional photoactivation microscopy. Journal of Microscopy **247**, 2–9.

Lin YT, Chen LJ, Herrfurth C, Feussner I, Li HM. 2016. Reduced biosynthesis of digalactosyldiacylglycerol, a major chloroplast membrane lipid, leads to oxylipin overproduction and phloem cap lignification in Arabidopsis. The Plant Cell **28**, 219–232.

Madsen SR, Kunert G, Reichelt M, Gershenzon J, Halkier BA. 2015. Feeding on leaves of the glucosinolate transporter mutant *gtr1gtr2* reduces fitness of *Myzus persicae*. Journal of Chemical Ecology **41**, 975–984.

Madsen SR, Olsen CE, Nour-Eldin HH, Halkier BA. 2014. Elucidating the role of transport processes in leaf glucosinolate distribution. Plant Physiology **166**, 1450–1462.

Matschi S, Hake K, Herde M, Hause B, Romeis T. 2015. The calcium-dependent protein kinase CPK28 regulates development by inducing growth phase-specific, spatially restricted alterations in jasmonic acid levels independent of defense responses in *Arabidopsis*. The Plant Cell **27**, 591–606.

McCully ME, Miller C, Sprague SJ, Huang CX, Kirkegaard JA. 2008. Distribution of glucosinolates and sulphur-rich cells in roots of field-grown canola (*Brassica napus*). New Phytologist **180**, 193–205.

Müller R, de Vos M, Sun JY, Sønderby IE, Halkier BA, Wittstock U, Jander G. 2010. Differential effects of indole and aliphatic glucosinolates on lepidopteran herbivores. Journal of Chemical Ecology **36**, 905–913.

Nintemann SJ, Hunziker P, Andersen TG, Schulz A, Burow M, Halkier BA. 2018. Localization of the glucosinolate biosynthetic enzymes reveals distinct spatial patterns for the biosynthesis of indole and aliphatic glucosinolates. Physiologia Plantarum **163**, 138–154.

Nour-Eldin HH, Andersen TG, Burow M, Madsen SR, Jørgensen ME, Olsen CE, Dreyer I, Hedrich R, Geiger D, Halkier BA. 2012. NRT/PTR transporters are essential for translocation of glucosinolate defence compounds to seeds. Nature **488**, 531–534.

Pickard WF. 2008. Laticifers and secretory ducts: two other tube systems in plants. New Phytologist **177**, 877–888.

Rogers LA, Campbell MM. 2004. The genetic control of lignin deposition during plant growth and development. New Phytologist **164**, 17–30.

Sarsby J, Towers MW, Stain C, Cramer R, Koroleva OA. 2012. Mass spectrometry imaging of glucosinolates in Arabidopsis flowers and siliques. Phytochemistry **77**, 110–118.

Schulz A, Kühn C, Riesmeier JW, Frommer WB. 1998. Ultrastructural effects in potato leaves due to antisense-inhibition of the sucrose transporter indicate an apoplasmic mode of phloem loading. Planta **206**, 533–543.

Sehr EM, Agusti J, Lehner R, Farmer EE, Schwarz M, Greb T. 2010. Analysis of secondary growth in the Arabidopsis shoot reveals a positive role of jasmonate signalling in cambium formation. The Plant Journal **63**, 811–822.

Shirakawa M, Ueda H, Shimada T, Hara-Nishimura I. 2016. FAMA: a molecular link between stomata and Myrosin cells. Trends in Plant Science **21**, 861–871.

Snegireva A, Chernova T, Ageeva M, Lev-Yadun S, Gorshkova T. 2015. Intrusive growth of primary and secondary phloem fibres in hemp stem determines fibre-bundle formation and structure. AoB Plants **7**, plv061.

Thangstad OP, Evjen K, Bones A. 1991. Immunogold-EM localization of myrosinase in *Brassicacea*. Protoplasma **161**, 85–93.

van Doorn WG. 2011. Classes of programmed cell death in plants, compared to those in animals. Journal of Experimental Botany **62**, 4749–4761.

Wang YY, Tsay YF. 2011. Arabidopsis nitrate transporter NRT1.9 is important in phloem nitrate transport. The Plant Cell **23**, 1945–1957.

Wille AC, Lucas WJ. 1984. Ultrastructural and histochemical studies on guard cells. Planta **160**, 129–142.

Xu D, Hanschen FS, Witzel K, Nintemann SJ, Nour-Eldin HH, Schreiner M, Halkier BA. 2017. Rhizosecretion of stele-synthesized glucosinolates and their catabolites requires GTR-mediated import in Arabidopsis. Journal of Experimental Botany **68**, 3205–3214.

Zhong R, Taylor JJ, Ye ZH. 1997. Disruption of interfascicular fiber differentiation in an Arabidopsis mutant. The Plant Cell **9**, 2159–2170.

Zhong R, Ye ZH. 1999. IFL1, a gene regulating interfascicular fiber differentiation in Arabidopsis, encodes a homeodomain-leucine zipper protein. The Plant Cell **11**, 2139–2152.